

Secondary Al-Si-Mg High-pressure Die Casting Alloys with Enhanced Ductility

DOMINIK BÖSCH, STEFAN POGATSCHER, MARC HUMMEL, WERNER FRAGNER, PETER J. UGGOWITZER, MATHIAS GÖKEN, and HEINZ WERNER HÖPPEL

Al-Si-Mg-based secondary cast alloys are attractive candidates for thin-walled high-pressure die castings for applications in the transport industry. The present study investigates the effect of manganese additions at high cooling rates on microstructure, mechanical properties, and on the dominating fracture mechanisms of alloy AlSi10Mg with an elevated iron concentration. Systematic variations of the Mn content from 0.20 to 0.85 wt pct at a constant Fe content of 0.55 wt pct illustrate the key changes in type, phase fraction, and shape of the Fe-containing intermetallic phases, and the corresponding influence on the alloy's ductility. For high-pressure die casting (HPDC), an optimal range of the Mn content between 0.40 and 0.60 wt pct, equivalent to a Mn/Fe ratio of approximately 1, has been identified. At these Mn and Fe contents, the high cooling rates obtained in HPDC result in the formation of fine and homogeneously distributed α -Al₁₅(Fe,Mn)₃Si₂ phase, and crack initiation is transferred from AlFeSi intermetallics to eutectic silicon. The study interprets the microstructure-property relationship in the light of thermodynamic calculations which reveal a significant increase in undercooling of the α -Al₁₅(Fe,Mn)₃Si₂ phase with increased Mn content. It concludes that the interdependence of the well-defined Mn/Fe ratio and the high cooling rate in HPDC can generate superior ductility in secondary AlSi10Mg cast alloys.

DOI: 10.1007/s11661-014-2700-8

© The Minerals, Metals & Materials Society and ASM International 2014

I. INTRODUCTION

THE majority of common high-pressure die casting (HPDC) alloys used in the transport industry are based on the aluminum-silicon-magnesium system due to its excellent casting abilities.^[1–3] As high ductility is absolutely mandatory for the implementation of aluminum in structural casting components, the alloy systems used today are produced from primary aluminum to keep impurities as low as possible and ensure good deformability. Several primary aluminum alloys have been developed for that purpose (e.g., Table I).

All the listed ductile alloys share the fact that their iron content is strictly limited to avoid the formation of undesired intermetallic phases, especially of the plate-shaped β -Al₃FeSi phase, whose detrimental effect on the

mechanical properties of Al-Si alloys is well known and has been described extensively.^[1–8] In contrast, usual secondary HPDC alloys possess iron contents of 1 to 2 wt pct, making them easy recyclable from different alloy families, but at the expense of an extremely poor deformability. While secondary aluminum alloys are beneficial for practical, economical, and 'carbon-footprint' points of view, their increased iron content is still the key obstacle to a widespread use in casting applications which require high ductility. Accordingly, various means and methods to prevent β -phase formation have been discussed in the literature.^[1–6] This prevention can be achieved either by influencing the solidification process^[3,7,8] or by adding so called 'iron correctors' such as Mn, Cr, and Co, which replace the β -phase by the favored polyhedral-shaped α -Al₁₅(Fe,Mn)₃Si₂-phase.^[1–6] For large-scale industrial usage, the Fe correction with Mn is accepted as the preferred economical solution due to its easy and uncritical implementation, and its relatively low price compared to other potential corrector elements. In addition, manganese helps to prevent die soldering during processing.

When typical secondary alloys with iron contents >1 wt pct are tried to be corrected with manganese, a new problem arises due to the so called sludge formation, meaning large intermetallic particles which may form at early stages in the casting process and influence the mechanical properties crucially.^[2,5–9] Therefore, secondary Al-Si-Mg alloys generally do not reach the ductility of primary Al-Si-Mg alloys due to the effect of Fe, even if present as favorable α -Al₁₅(Fe,Mn)₃Si₂-phase. Many investigations have sought a better

DOMINIK BÖSCH, formerly with the Department of Materials Science and Engineering, Institute 1: General Materials Properties, University Erlangen-Nürnberg, 91058 Erlangen, Germany, is now Development Engineer, with the AUDI AG, 85045 Ingolstadt, Germany. STEFAN POGATSCHER, Postdoc, is with the Laboratory of Metal Physics and Technology, Department of Materials, ETH Zurich, 8093 Zurich, Switzerland. MARC HUMMEL, Development Engineer, is with the AUDI AG, 74148 Neckarsulm, Germany. WERNER FRAGNER, Head of Corporate Technology, is with the Austria Metall AG (AMAG), 5282 Ranshofen, Austria. PETER J. UGGOWITZER, Professor, is with the Laboratory of Metal Physics and Technology, Department of Materials, ETH Zurich. MATHIAS GÖKEN, Professor, and HEINZ WERNER HÖPPEL, Senior Scientist, are with the Department of Materials Science and Engineering, Institute 1: General Materials Properties, University Erlangen-Nürnberg. Contact e-mail: hoeppel@ww.uni-erlangen.de.

Manuscript submitted September 16, 2014.

Article published online December 10, 2014

Table I. Conventional Primary Casting Alloys with High Ductility Based on the Aluminum-Silicon-Magnesium System (Element Content in Weight Percent)

Alloy	Si	Mg	Fe	Mn	Cu	Ti	Sr
Silafont 36 Rheinfelden	9.5 to 11.5	0.1 to 0.5	0.15 max	0.5 to 0.8	0.03 max	0.15 max	0.01 to 0.02
Aural 2 Magna	10 to 11	0.1 to 0.6	0.15 to 0.20	0.45 to 0.55	—	0.04 to 0.08	0.01 to 0.016
A367 Mercury Castings	8.5 to 9.5	0.3 to 0.5	0.25 max	0.25 to 0.35	0.25 max	—	0.05 to 0.07
A368 Mercury Castings	8.5 to 9.5	0.1 to 0.3	0.25 max	0.25 to 0.35	0.25 max	—	0.05 to 0.07

understanding of the quantity of Mn necessary to fully tie a specific amount of Fe into the α -phase, and how much Mn and Fe are tolerable when sludge formation should be avoided. However, almost all of these studies have been carried out on samples produced on a laboratory scale and/or using gravity mold casting.^[4–6,10,11] Only little work has been done to comprehend how the much higher solidification rate in HPDC processes affects the formation of the Fe bearing phases and which ratio of Fe to Mn should be chosen to maintain high ductility even in alloys containing increased Fe content. Recently Ji *et al.*^[12] published their investigations on how varied Fe and Mn concentrations affect the phase formation and the mechanical properties of Al-Mg-Si alloys in HPDC. However, their findings for the Al-Mg-Si alloy family^[12] cannot be directly related to Al-Si-Mg alloys, because they differ in their solidification sequence and microstructure. The same applies to the patent application of Lumley *et al.*, who determined Mn/Fe ratios for Al-Si-Cu alloys.^[13]

The objective of the present study was to fill the gap between iron-free primary alloys and strongly iron-containing (>1 wt pct) secondary alloys by investigating the intermediate window and to develop an alloy system with the recycling skills of secondary and the mechanical abilities of primary aluminum alloys. An iron content of 0.55 wt pct was selected, providing the opportunity to use secondary aluminum, *i.e.*, Al of low purity, with its advantage of reduced costs and attractive ecological footprint. However, the mechanical properties must be retained. Thus, the ambition of our study was to evaluate an optimal chemical Mn content for AlSi10Mg (with 0.55 wt pct Fe) for use in HPDC processing, and specifically to (i) clarify the effect of Mn on the type, fraction, and shape of the dominant AlFe(Mn)Si intermetallics; (ii) generate a better understanding of crack initiation under tensile loading; and (iii) evaluate the mechanical properties, with special emphasis on ductility, where we aim to sustain the excellent deformation behavior of primary Al-Si-Mg alloys, *i.e.*, an elongation to fracture of >10 pct.

II. EXPERIMENTAL

The alloy design was guided by the following targets: (i) good castability, ensured by a high Si content of about 10 wt pct; (ii) high Fe content of 0.55 wt pct, enabling the use of high Al-scrap fractions; and (iii) systematic variation of the Mn content in order to cover a broad range of intermetallic AlFe(Mn)Si emergence, from β -phase at low-Mn content to sludge formation at

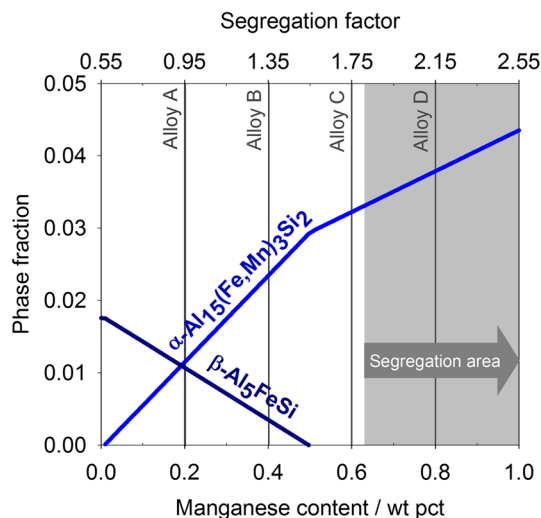


Fig. 1—Phase fraction of α -Al₁₅(Fe,Mn)₃Si₂- and β -Al₅FeSi-phase in alloy AlSi10.5Mg0.4Fe0.55-Mn at 773 K (500 °C), calculated for equilibrium condition. The gray area depicts the prediction of sludge formation (SF >1.8).

very high Mn additions. Even if the overarching problems of sludge formation are mainly related to reduced tool life and machinability, its effect on microstructure and mechanical properties is also of particular interest. Sludge is known to occur at a critical concentration of Fe, Mn, and Cr. It can be estimated by a critical segregation factor ($SF_{crit} \approx 1.8$), with $SF = Fe + 2Mn + 3Cr$ (in wt pct).^[4,9,14,15] The Fe content of 0.55 wt pct makes it possible to choose different amounts of Mn without exceeding the critical SF limit. Thermodynamic calculations in equilibrium and non-equilibrium conditions have been carried out using Pandat software^[16] to evaluate the amount of α - and β -phase at different Mn concentrations. The results of the simulations for AlSi10.5Mg0.4Fe0.55-Mn are shown in Figure 1, together with the corresponding segregation factors.

Four different alloys A-D were chosen with increasing Mn content (0.2, 0.4, 0.6, and 0.85 wt pct, respectively) including the transition from the α - plus β -phase field to the solely α -phase area (Table II). According to the thermodynamic modeling, the two low-Mn alloys A and B should form the detrimental β -phase, whereas alloy D is assumed to show the appearance of large sludge α -particles (SF > 1.8). The composition of alloy C is designed just in between so that neither β -phase nor sludge should appear.

The selected chemical compositions were cast into sheets of 3-mm thickness, 60-mm width, and 220-mm length,

Table II. Chemical Composition Measured by Spectral Analysis, Segregation Factor (SF), and Expected Iron-Containing Phases of the Investigated Alloys (Element Content in Weight Percent)

Alloy	Si	Mg	Fe	Mn	SF	Phases (Calculated)
A	10.54	0.41	0.55	0.20	0.95	$\text{Al}_{15}(\text{FeMn})_3\text{Si}_2 + \text{Al}_5\text{FeSi}$
B	10.62	0.42	0.55	0.41	1.37	$\text{Al}_{15}(\text{FeMn})_3\text{Si}_2 + \text{Al}_5\text{FeSi}$
C	10.34	0.40	0.55	0.62	1.79	$\text{Al}_{15}(\text{FeMn})_3\text{Si}_2$
D	10.46	0.41	0.52	0.85	2.22	$\text{Al}_{15}(\text{FeMn})_3\text{Si}_2$ (sludge)

using a 400 t vacuum-assisted die casting machine. The desired compositions were achieved by alloying commercial pure aluminum 99.8. The melt temperature during casting was 983 K (710 °C), and the mold was heated by oil circulation to approximately 393 K (120 °C). The microstructure of the alloys was characterized using a Zeiss Crossbeam 1540EsB scanning electron microscope (SEM) equipped with energy dispersive X-ray spectroscopy (EDS) and focused ion beam (FIB). Samples of $10 \times 10 \times 3 \text{ mm}^3$ were cut from the middle of the casting sheet and polished for microstructural characterization. Good contrast for the intermetallic phases was obtained using a quadrant back scattering detector (QBSD). EDS analysis was carried out using an acceleration voltage of 20 kV. Characterization of the distribution, size, and fraction of intermetallic particles was performed with Matlab Software and ImageJ. Ten random SEM pictures (500 \times) were evaluated for each alloy. FIB cuts were carried out very close to the fracture region of tensile test specimens. By avoiding the conventional polishing route, it was assured that no preparation artifacts remained on the surface, and by taking SEM pictures directly after FIB milling, the sample could be examined in an evacuated environment without exposure to atmosphere. The images after FIB milling were taken with a secondary electron (SE) and in-lens detector (IL), as the QBSD detector could not be used in combination with the FIB gun. Mechanical properties were determined in tensile tests according to DIN EN ISO 6892 using a Zwick & Roell Z020 tensile test machine with a 20 kN load cell and TestExpert software. Flat tensile samples with $10 \times 3 \text{ mm}^2$ cross section were cut from the sheets after undergoing T7 tempering, including solution heat treatment at 733 K (460 °C) for 1 hour, water quenching, and annealing at 493 K (220 °C) for 2 hours. The tests were performed at room temperature at a strain rate of 0.008/s and an extensometer gage length of 30 mm. For each alloy, nine tensile specimens were tested, and average values for the yield strength, ultimate tensile strength, uniform elongation, and elongation to fracture were calculated. Differential scanning calorimetry (DSC) was performed on a Mettler Toledo DSC 1 using cooling rates of 5, 10, 50, and 100 K/min for flat specimens of 22 mg. Measurements were conducted between 973 K and 573 K (700 °C and 300 °C) in alumina pans with an empty pan on the reference platform and employing an argon gas flow of 30 mL/min. An additional setup was deployed to realize the extremely high cooling rates occurring in HPDC, in which about 4 g of alloy material was poured by means of a levitation system into a copper mold equipped with a thermocouple with data capture of 1 kHz, resulting in cooling rates of approximately $2.5 \times 10^4 \text{ K/min}$.

III. RESULTS

A. Microstructure

Figure 2 shows the microstructure of each of the four alloys in the middle of the casting sheet and illustrates the effect of an increasing Mn content. It is obvious that the undesired platelet-shaped β -phase (which appears in needle shape in 2D) is only detectable in alloy A, with the lowest Mn content of 0.2 wt pct. When the Mn content is increased to 0.4 wt pct (alloy B), the β -phase has completely disappeared but is replaced by small polyhedral particles that were analyzed with EDS as the α - $\text{Al}_{15}(\text{Fe,Mn})_3\text{Si}_2$ phase (Table III). A further increase in Mn produces a remarkable refinement of these primary intermetallic particles (alloy C), whereas alloy D, with the highest Mn concentration, shows the occurrence of large α -particles that are attributed to sludge formation during casting (Figure 1).

The phase fraction of intermetallic compounds increases with the addition of Mn and corresponds well to thermodynamic calculations (Figure 3(a)). However, raising the Mn content does result not only in a higher phase fraction of the α -phase but also in an obvious change in its size (Figure 3(b)). The median of the minimum feret diameter of the particles in alloy B, with 0.4 pct Mn (2.25 μm), is reduced by one-third through an increase to 0.6 pct Mn in alloy C, and a further slight decrease in diameter is observed for alloy D. For Figure 3(b), only phases up to a maximum area of 25 μm^2 have been evaluated to avoid falsification due to very large sludge particles in alloy D. Note that the distribution of the cumulative frequency is quite similar for alloys C and D but deviates remarkably for alloy B. Further details of the diameter distribution are given in Table IV. Because alloy A shows only little primary α -phase, no statistically meaningful measurements could be carried out.

In addition to the clearly visible primary α - and β -phases, some fine intermetallic phases (IMP) can be seen in Figure 2. Their size is very small, making it impossible to detect their accurate chemical compositions using SEM/EDS. According to thermodynamic calculations, it may be assumed that they are formed during the eutectic reaction and are primarily of type π - $\text{Al}_8\text{FeMg}_3\text{Si}_6$.

B. Mechanical Properties

Figure 4 shows the tensile test results for the alloys in T7 temper. The yield strength of the four alloys is in the range of 150 MPa and is not significantly affected by the different Mn contents, just like the ultimate tensile strength, which scatters around 225 MPa. However, a

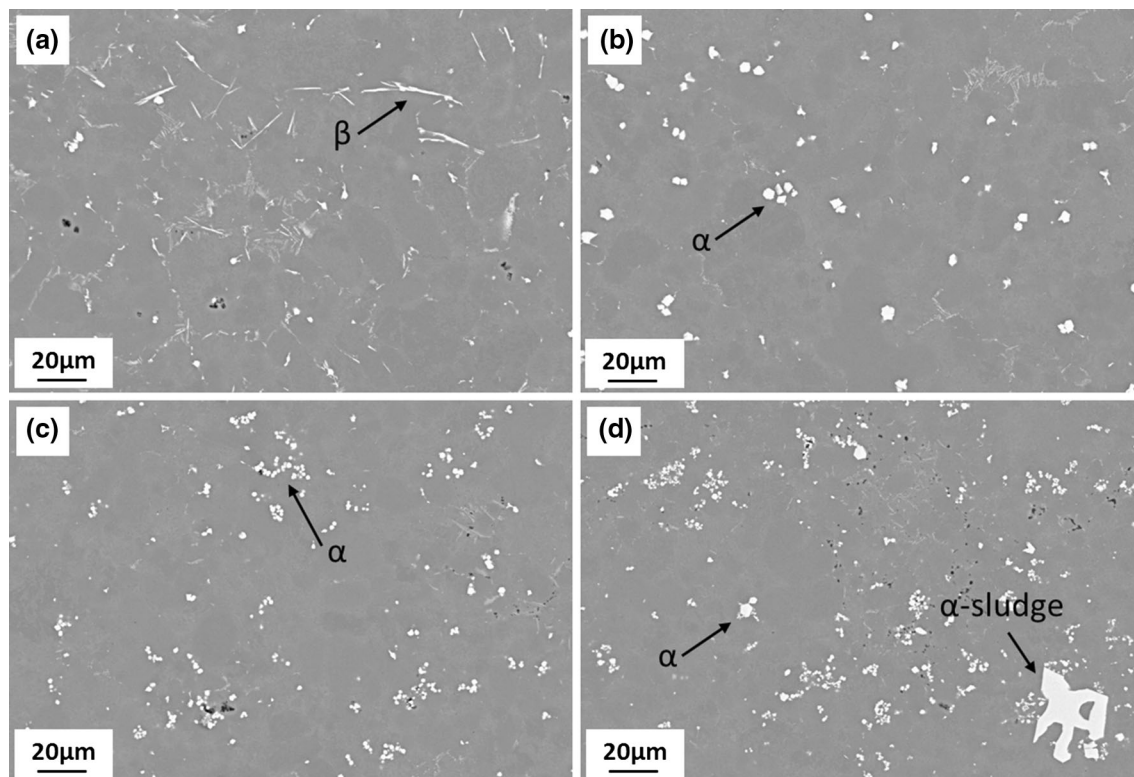


Fig. 2—Iron- and manganese-containing phases of the four investigated alloys (A-D; see Table II). The transition from platelet-shaped to globular phases between alloys A and B and the occurrence of large α -phase (sludge) in alloy D are evident.

Table III. Theoretical and Measured Chemical Compositions of α -Al₁₅(Fe,Mn)₃Si₂ and β -Al₅FeSi, Measurements by EDS

Phase	Element Concentration (at. pct)			
	Al	Si	Mn	Fe
α -Al ₁₅ (Fe,Mn) ₃ Si ₂	Theoretically	75.0	10.0	$\Sigma_{(Mn+Fe)}$ 15.0
	Measured	75.8	12.2	8.4 3.6
β -Al ₅ FeSi	Theoretically	71.4	14.3	— 14.3
	Measured	70.7	20.8	1.8 6.7

significant influence can be seen on the uniform elongation and the elongation to fracture. The alloy modifications B and C exhibit an elongation to fracture of about 12 pct, which is considerably higher than that of alloys A and D; they also show an increase in uniform elongation. The stress-strain curves are similar in shape, indicating that the alloys have the same yield strength and UTS and therefore identical strain-hardening behavior, which is confirmed by a strain-hardening exponent between 0.18 and 0.19 for all investigated alloys. However, while the uniform elongation is only slightly changed, it clearly turns out that the elongation to fracture is significantly different between the four alloys.

C. Fracture Behavior

To investigate the effect of intermetallic particles of different shape and size on mechanical behavior, and in

particular on the fracture mechanism, a SEM study, which also employs a FIB as a sample preparation tool, was carried out. Based on the microstructural observations presented in Figure 2, three of the four alloys were chosen for FIB investigations, namely A, B, and D. Because alloy C shows a morphology, which although more refined, is comparable to that of alloy B, and similar mechanical properties, no significant difference in the fracture mechanisms of these two alloys was expected. Using a FIB, some microns of the sample surface perpendicular to the fracture surface were removed to open the view inside the material (Figure 5). Afterward, the exposed surface was examined directly inside the vacuum chamber.

Figure 6 shows two SEM pictures of the microstructure close to the fracture zone for each of the three observed alloys. A dual consideration is essential to gain a comprehensive view of the complete microstructure, with the in-lens detector (IL) highlighting the eutectic Si particles and the secondary electron detector (SE) monitoring the α - and β -phases. The first letter of the image designation indicates the investigated alloy, while the following notation refers to the detector used. The images show a section near to the fracture surface (white rectangle in Figure 5).

From Figure 6 A-SE, it is obvious that the β -Al₅FeSi phase, in white, exhibits needle/platelet-like morphology as described above. The Si particles, shown black in A-IL, were spheroidized during heat treatment and are therefore globular shaped. For alloy A, it is apparent that most of the microcrack and cavity formation can be

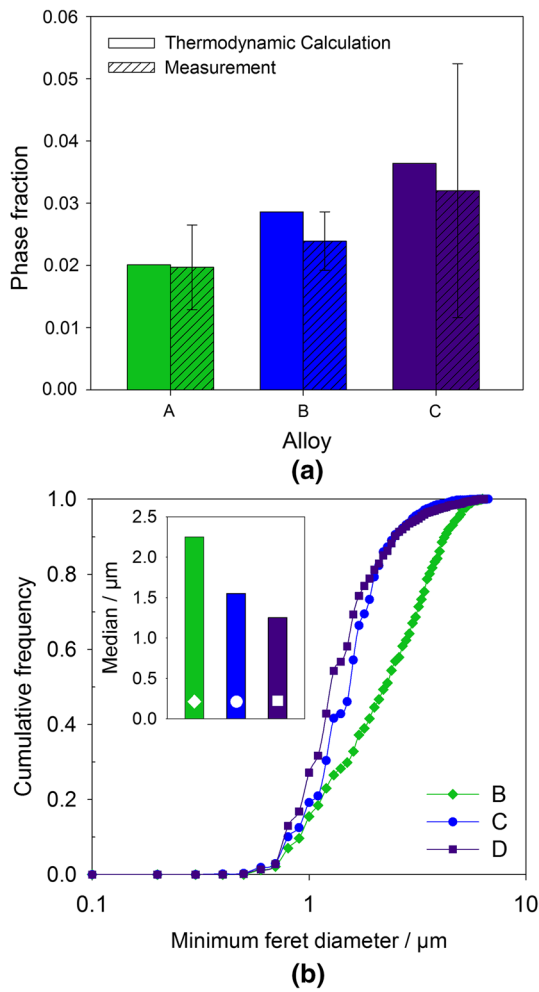


Fig. 3—(a) Phase fraction and (b) cumulative size frequency of the minimum feret diameter of the α -particles (excluding sludge). The inset shows the median of the minimum feret diameter for alloys B, C, and D.

Table IV. Median Diameter d_{50} and 95 Pct Confidence Interval ($d_{2.5}$ and $d_{97.5}$) of the α - $\text{Al}_{15}(\text{Fe},\text{Mn})_3\text{Si}_2$ Particles

Alloy	Median Diameter d_{50} (μm)	Confidence Interval 95 Pct	
		Lower Limit $d_{2.5}$ (μm)	Upper Limit $d_{97.5}$ (μm)
A	—	—	—
B	2.25	0.7	5.2
C	1.54	0.6	3.5
D	1.24	0.7	4.1

attributed to the fracture of the β -platelets (white arrows). While microcrack formation takes place *via* fragmentation of β -platelets oriented roughly parallel to the loading direction, which is from top to bottom in all images, decohesion at the β -phase/matrix interface can be observed at the β -platelets oriented roughly perpendicular to the loading direction. Only few microcracks emerge at the spheroidized eutectic Si particles (marked by arrows in Figure 6 as examples). When the β -

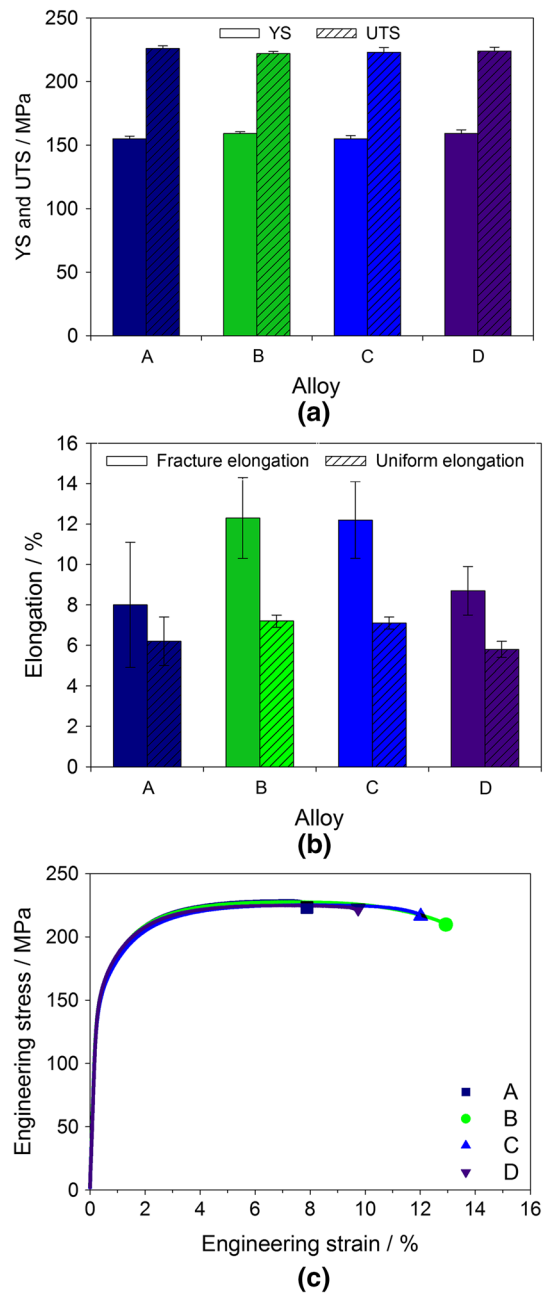


Fig. 4—(a) Yield strength (YS) and ultimate tensile strength (UTS); (b) uniform elongation and elongation to fracture in T7 condition; (c) representative stress–strain curves of the four alloys (particular symbols have been added for reasons of distinction).

platelets are transformed into globular α - $\text{Al}_{15}(\text{Fe},\text{Mn})_3\text{Si}_2$ phase by adding Mn as in alloy B (and C), crack initiation takes place at Si particles and only few intermetallic α - $\text{Al}_{15}(\text{Fe},\text{Mn})_3\text{Si}_2$ phases act as failure initiation sites (Figure 6, B-IL and B-SE). Again, two different mechanisms are apparent: cracking of the Si particles and particle/matrix decohesion (marked by arrows in Figure 6). Obviously, the predominant damage mechanism can be related to the eutectic Si particles and not the Fe-containing intermetallic phases. Thus, the influence of the latter is of minor importance. When the weighted sum of Fe and Mn is increased over the

postulated limit of the segregation factor ($SF > 1.8$) and large primary intermetallic particles are formed in the casting parts, as in alloy D, the dominating crack initiation site switches back to Fe-containing intermetallic phases, but only to the large sludge particles

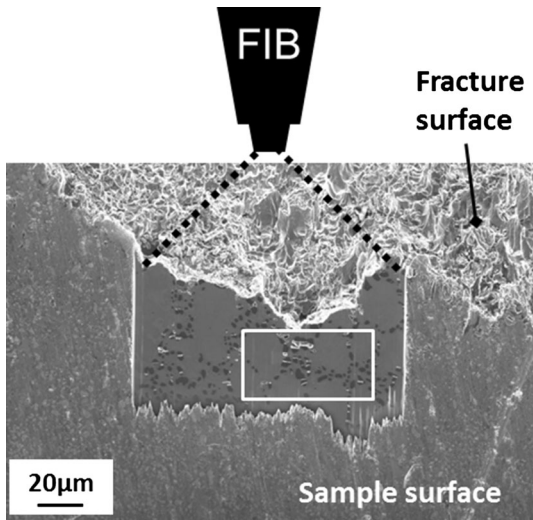


Fig. 5—FIB sample preparation and imaging of the fracture behavior. The white rectangle displays the investigated sample area (see Fig. 6).

(marked by arrows in Figure 6). Similar to the situation in alloy B, the small globular α - $\text{Al}_{15}(\text{Fe},\text{Mn})_3\text{Si}_2$ particles do not act as crack initiators, but few small voids also formed close to spheroidized Si particles. Image D-SE clearly shows that the large sludge particles tend to crack in multiple ways during tensile loading, resulting in the formation of huge cavities in between.

IV. DISCUSSION

A. Influence of Mn Content on the Microstructure in HPDC

As expected from thermodynamic modeling (Figure 1), the intermetallic phases occurring in the investigated alloys (Figure 2) depend essentially on the ratio and cumulative amount of Fe and Mn. While alloy A features the undesired platelet-shaped β - Al_5FeSi phase, alloy B and C exhibit the favored α - $\text{Al}_{15}(\text{Fe},\text{Mn})_3\text{Si}_2$ phase that forms in polyhedral morphology. In alloy D, the fine dispersed α -phase is also present, but some large α -particles (sludge) have also formed during the casting process. While it can be assumed that the small primary β - and α -phases solidify in the die, the sludge particles are supposed to already emerge in the shot sleeve when the hot melt is poured into the cold casting chamber of the HPDC machine. Similar observations on the formation of Fe- and Mn-containing

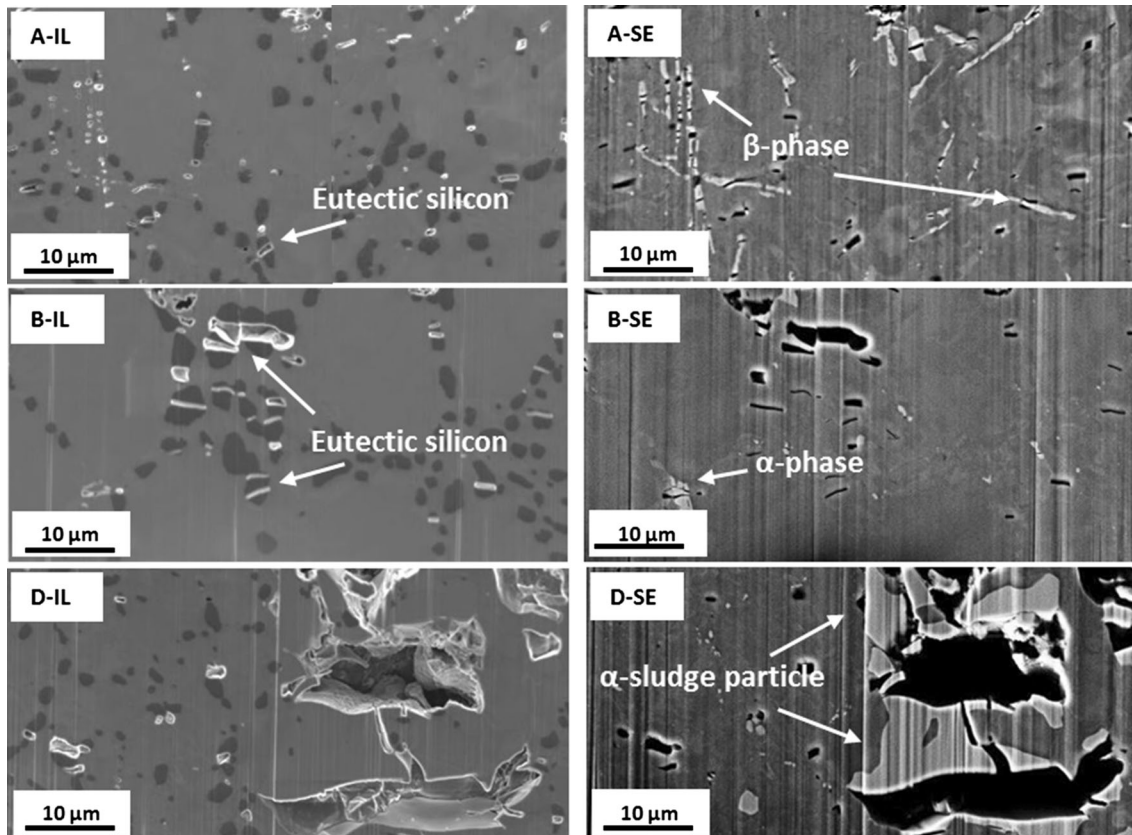


Fig. 6—FIB cross section near the fracture surface of alloys A, B, and D. Images were taken with an in-lens detector (IL) and a secondary electron detector (SE). Arrows indicate the main cavity formation sites.

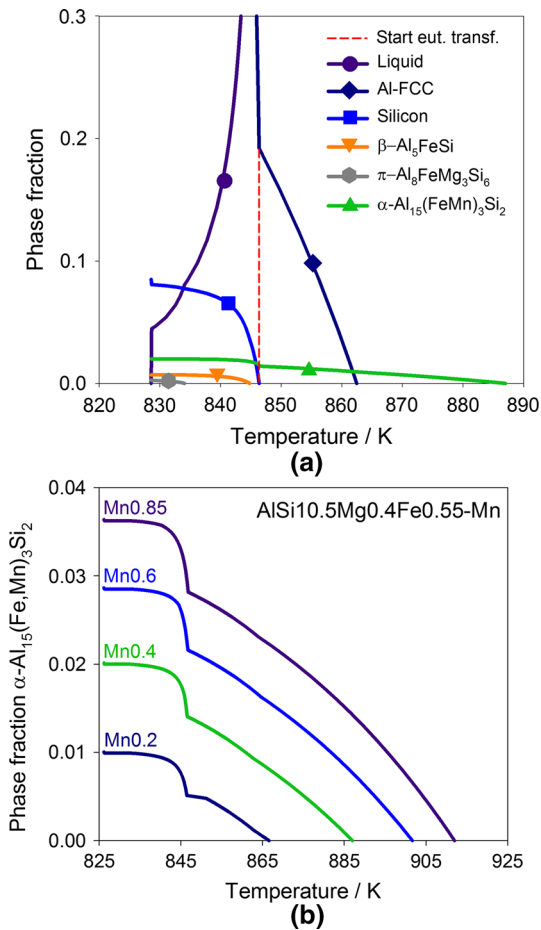


Fig. 7—(a) Solidification of alloy B in non-equilibrium conditions according to Scheil (particular symbols have been added for reasons of distinction). (b) Solidification of the α - $\text{Al}_{15}(\text{Fe},\text{Mn})_3\text{Si}_2$ phase for the investigated alloys A-D.

intermetallics in aluminum alloys have been reported in References 4, 12, 15. Nevertheless, it is worth noting that the critical segregation factor is temperature dependent, and thus, SF_{crit} is influenced by the casting temperature and the thermal conditions in the shot sleeve. However, the processing conditions are well reflected by $\text{SF}_{\text{crit}} = 1.8$ in our case.

While the increase in the Mn content from alloys A to B generates a considerable change in the primary intermetallic phase from β to α , further addition of Mn (alloys B to C) results in significant refinement of the α -particles (Figures 2 and 3(b)). However, an additional increase from 0.6 to 0.85 pct for alloy D does only slightly change the α -particle diameter if large sludge particles ($>25 \mu\text{m}^2$) are excluded. To understand these microstructural changes, it is helpful to consider the solidification sequence of the investigated alloys, shown in Figure 7(a) using alloy B as an example. It is obvious that the first phase to precipitate from the melt is the α - $\text{Al}_{15}(\text{Fe},\text{Mn})_3\text{Si}_2$ phase at approximately 887 K (614 °C). The second phase which solidifies is FCC aluminum at about 862 K (589 °C), while all other phases set only during the eutectic transformation, which starts at 846 K (573 °C). The amount of α -

intermetallics increases with increasing Mn content, as shown in Figure 7(b).

As shown in Figure 7(b), not only does the phase fraction of α - $\text{Al}_{15}(\text{Fe},\text{Mn})_3\text{Si}_2$ increase with increasing Mn concentration but its liquidus temperature is also shifted to higher values. Raising the Mn content from 0.2 to 0.8 wt pct leads to a shift of the α -liquidus of more than 40 K. Let us therefore assume hypothetically that, for otherwise identical cooling conditions (high cooling rates in HPDC), the undercooling of the α - $\text{Al}_{15}(\text{Fe},\text{Mn})_3\text{Si}_2$ phase inside the die is increased by the magnitude of the shift of its solvus temperature. This would enlarge the undercooling by about 15 K when the Mn content is increased from 0.4 wt pct (alloy B) to 0.6 wt pct (alloy C), and produce a higher nucleation rate, which in turn may explain the observed microstructural refinement.^[17] The reason for the minimal further refinement at an Mn content of 0.85 wt pct (alloy D) can be explained by the formation of the ultralarge α -sludge particles in the shot sleeve. When part of the Fe and Mn content is already consumed inside the shot sleeve, the concentration of these elements in the melt that enters the die is reduced, and the melt composition and the undercooling of the α -phase are expected to be close to the range of alloy C.

Very recently Ji *et al.*^[12] investigated the effect of different Fe concentrations on phase formation in $\text{AlMg6.2Si2.2Mn0.54}$ processed *via* HPDC. A quantitative re-examination of their published microstructures with ImageJ indicates a similar effect. At their lowest Fe content (0.21 wt pct), the α - AlFeMnSi phase appears as globular particles, and an increase in the iron level to 0.62 wt pct generates a reduction of their minimum feret diameter from 0.84 μm to approximately 0.46 μm ; see Figure 8(a). These findings agree with the results presented in Figure 3(b). A further increase of Fe to 1.24 wt pct results in the occurrence of large sludge particles which grow bigger and more numerous at the highest Fe concentration of 1.86 wt pct. If the large sludge particles are excluded, as in the evaluation made for Figure 3(b), the average particle size stays constant for an Fe content above a certain limit, similar to what is reported here for the AlSi10Fe0.5 alloy with different Mn concentrations. Thus, the observed phenomenon seems to occur generally and not only for a specific alloy.

The hypothetical assumption of an increased undercooling of the α -phase can also be applied to the $\text{AlMg6.2Si2.2Mn0.54}$ alloy system. Thermodynamic calculations show clearly that an increase in the Fe content from 0.21 to 1.24 wt pct accompanies a shift of the α -liquidus from 901 K to 940 K (628 °C to 667 °C) (Figure 8(b)). A further increase to 1.86 wt pct Fe no longer changes the liquidus temperature but leads to a decline in the α -phase fraction, which can be explained by the limited Mn and Si content of the alloy and the consequential formation of $\text{Al}_{13}\text{Fe}_4$.^[12] These results perfectly match the observations made in our $\text{AlSi10.5Mg0.4Fe0.55}$ system.

The presented hypothesis of higher undercooling with increased liquidus temperature of the α -phase implies that α - $\text{Al}_{15}(\text{Fe},\text{Mn})_3\text{Si}_2$ does not solidify as the first

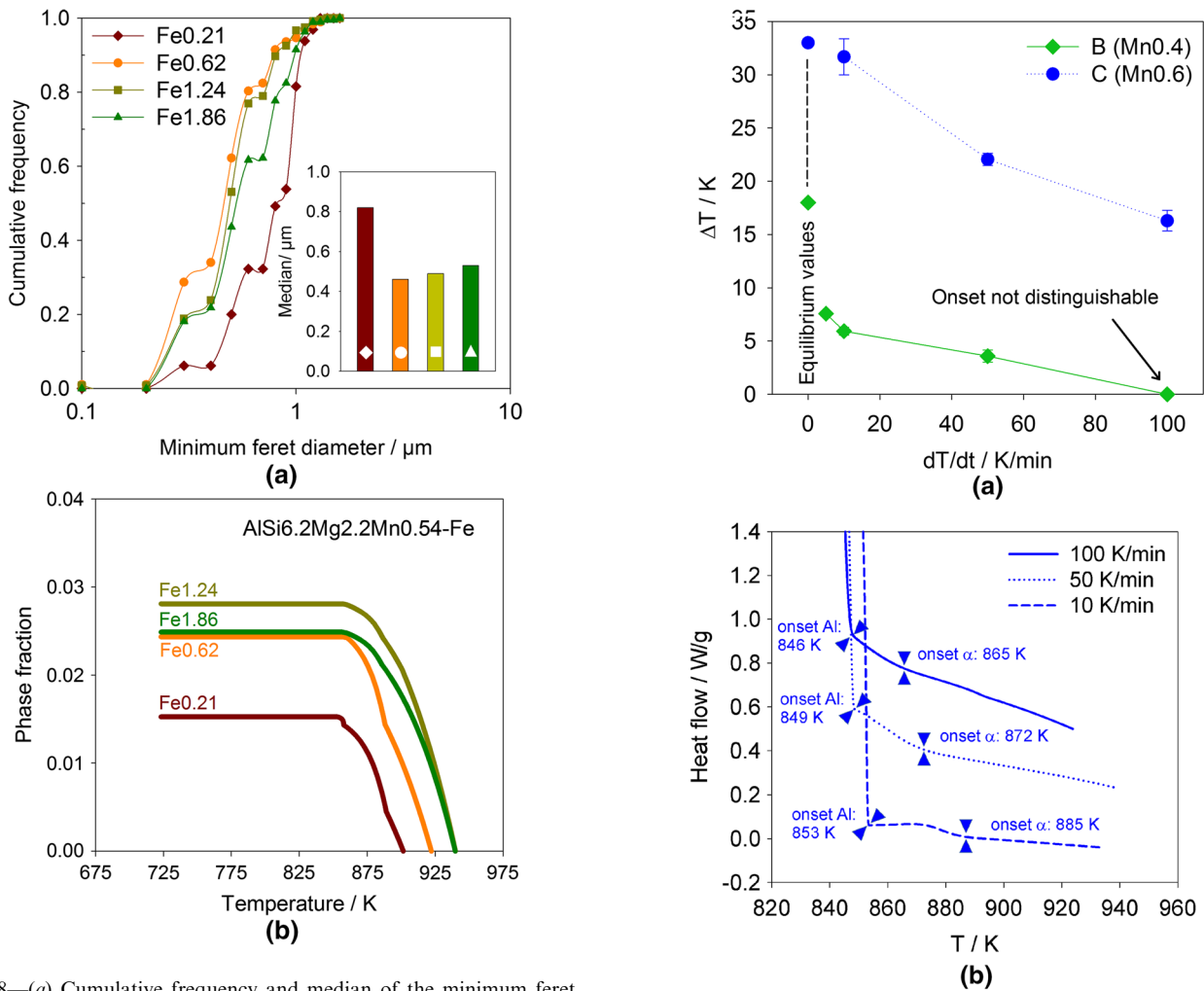


Fig. 8—(a) Cumulative frequency and median of the minimum feret diameter of α -AlFeMnSi particles (excluding sludge), and (b) thermodynamic calculations of α -fraction (according to Scheil) as a function of the Fe content in alloy AlMg6.2Si2.2Mn0.54 (particle size data evaluated from images presented in Ref.[15]).

phase from the melt, as indicated by the thermodynamic modeling, because then a coarsening of the intermetallic particles with increasing Mn content would be expected. A refinement due to higher Mn content only seems reasonable if cooling is so fast that the intermetallic phases solidify only when FCC aluminum solidification begins, with its associated release of heat of fusion. This sequence would generate the proposed increase in the undercooling and nucleation rate. To support this assumption, different thermo-analyses were carried out. Figure 9(a) shows the temperature difference (ΔT) between the onset of the α -Al₁₅(Fe,Mn)₃Si₂ peak and the FCC aluminum for different cooling rates and alloys B and C measured by DSC. In order to illustrate the thermal effects of different cooling rates on α -Al₁₅(Fe,Mn)₃Si₂ and FCC-Al solidification, the results of DSC measurements performed at cooling rates of 10, 50, and 100 K/min are exemplarily shown for alloy C (0.6 wt pct Mn) in Figure 9(b).

It is apparent that for both alloys, the difference between the onset temperatures of α -Al₁₅(Fe,Mn)₃Si₂ and FCC aluminum decreases as the cooling rate

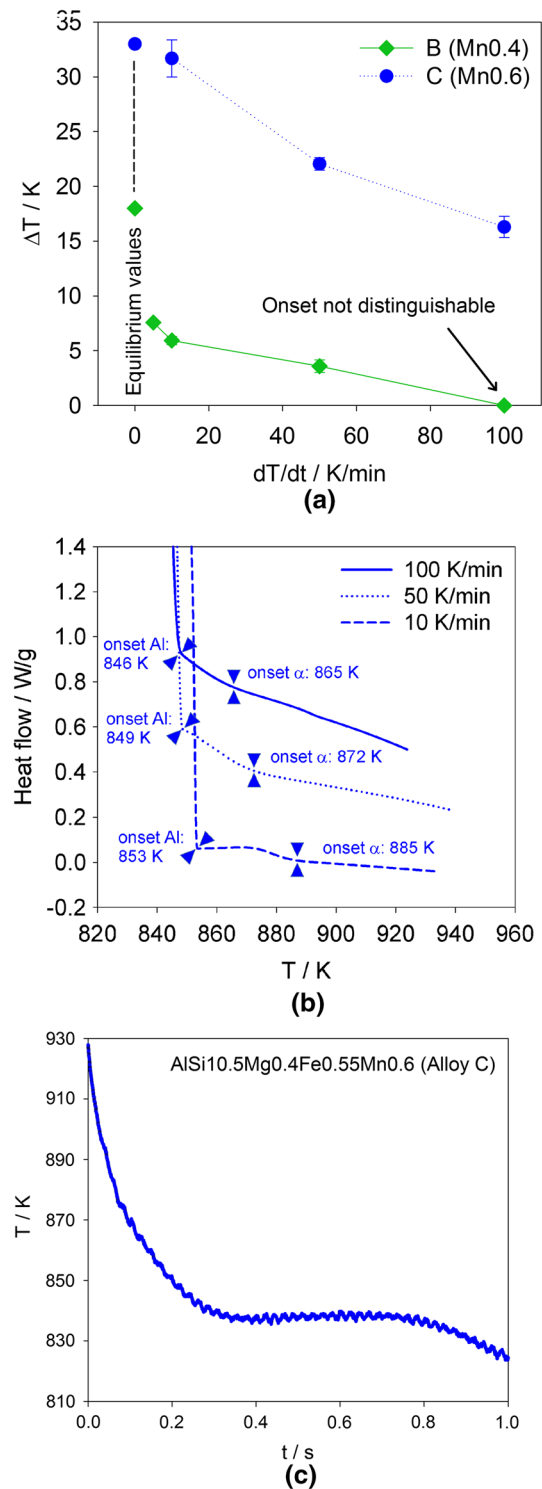


Fig. 9—(a) Temperature difference ΔT between the onset temperatures of α -Al₁₅(Fe,Mn)₃Si₂ and FCC aluminum for alloys B and C measured by DSC for low to medium cooling rates. (b) Displacement of the temperature difference ΔT for different cooling rates exemplarily shown for alloy C. (c) Temperature-time progression for fast cooling ($\sim 2.5 \times 10^4 \text{ K/min}$) by levitation casting of alloy C with 0.6 wt pct Mn.

increases. For the alloy B with 0.4 wt pct Mn, a cooling rate of 100 K/min is already sufficient to shift the temperature of α -phase formation to the FCC aluminum

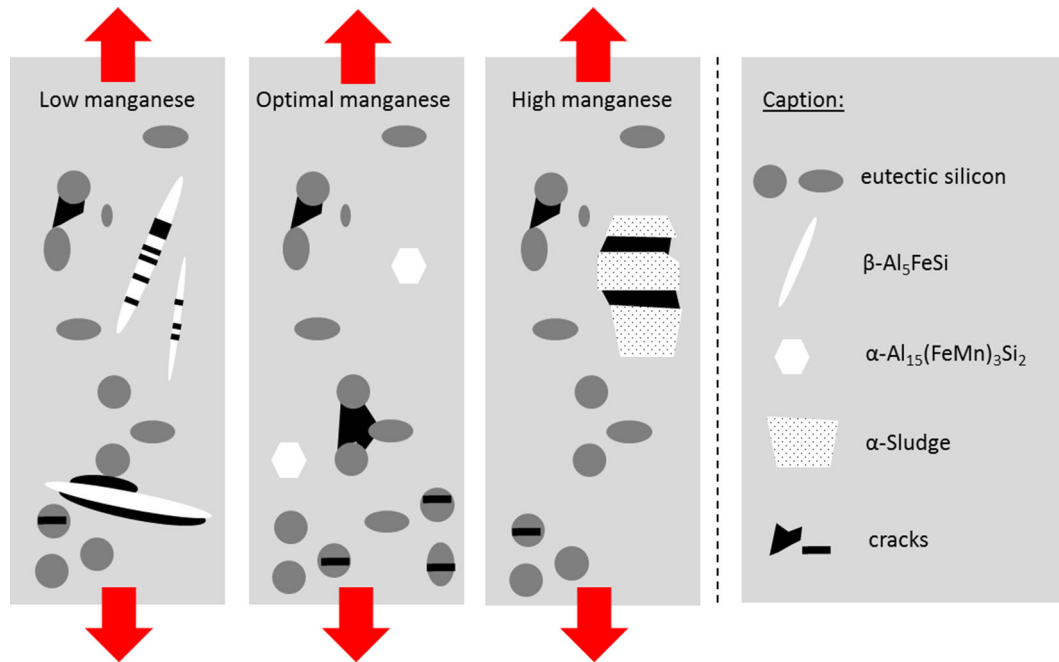


Fig. 10—Principal crack initiation in alloys with low, optimal, and high Mn content. The red arrows mark the loading direction: microcracks and cavities are depicted in black, silicon particles in gray, and iron/manganese intermetallics in white (Color figure online).

solidification temperature. For 0.6 wt pct Mn, the initial equilibrium difference is twice the value of 0.4 wt pct Mn, and the maximum in cooling rate performable in DSC of 100 K/min is not enough to shift the α - $\text{Al}_{15}(\text{FeMn})_3\text{Si}_2$ onset together with the onset of FCC aluminum, but the trend toward lower values is obvious. Because the solidification rate in HPDC is in the range of $>10^4$ K/min for thin-walled castings,^[18] an entire closing of the gap between α - $\text{Al}_{15}(\text{FeMn})_3\text{Si}_2$ and FCC aluminum solidification can be assumed. Similar observations were made by Belmares-Perales *et al.*^[19] They investigated AlSi7.3Cu3.5 alloys and report that β - AlFeSi precipitation approaches the solidification onset of eutectic Al-Si when the cooling rate is increased. Figure 9(c) also shows the temperature–time progression for alloy C for very high cooling rate (2.5×10^4 K/min) in the levitation setup, and no thermal effect of α - $\text{Al}_{15}(\text{FeMn})_3\text{Si}_2$ formation is detected.

B. Influence of the Microstructure on Fracture Mechanisms and Ductility

The described changes in the microstructure based on the different Mn levels are compatible with the observations from the tensile tests. The yield strength and ultimate tensile strength levels are not influenced by Mn additions since they only affect the Fe-containing intermetallic phases and not the alloy's matrix. β - Al_5FeSi and α - $\text{Al}_{15}(\text{Fe,Mn})_3\text{Si}_2$ do not act as hardening phases because of their large average distance and low volume content.^[20] Figure 4(b), however, discloses a considerable effect of the intermetallic phases on fracture elongation. Alloys A and D reach fracture elongations of about 8 pct and are significantly less ductile than alloys B and C with roughly 12 pct (Figure 4).

While the shape of the stress–strain curves is almost identical for all alloys until the ultimate tensile strength is reached and the uniform elongation is only slightly enhanced in alloys B and C, major differences appear after the samples have undergone necking and triaxial loading is induced. Even if the variance is relatively high and the error bars might overlap, the maximum elongation values which show the real materials potential are remarkably higher in alloys B and C. The scattering is also quite typical for casting applications where several internal defects can arise during processing and solidification.

As expected, neither the platelet-shaped β phase nor the large α -sludge particles are beneficial for ductility. At increasing Mn content, a decisive change in fracture initiation takes place, which was revealed by the FIB/SEM study on fractured tensile samples (Figure 6). Schematic drawings of the principal crack initiation sites are shown in Figure 10.

In an alloy with insufficient low-Mn content (*i.e.*, alloy A), the platelet-shaped β - Al_5FeSi phase acts as the main crack initiation site. β -phases oriented in the loading direction break into several fragments and voids are formed in between, whereas at β -phases perpendicular to the loading direction, microcracks are formed by decohesion of the β -phase/matrix interface.^[21] Only sporadic microcrack formation can be attributed to cleavage of eutectic Si particles or Si particle/matrix decohesion. However, this mechanism becomes predominant for an alloy with an optimal Mn content (alloys B and C). The α - $\text{Al}_{15}(\text{FeMn})_3\text{Si}_2$ phase is of comparable size and morphology to the Si particles but appears in considerably smaller numbers, and its effect on crack formation becomes minor. No change in the fracture mechanism takes place when the Mn content is

increased and the intermetallic phases become even more finely dispersed (alloy C) until the Mn content exceeds the limit for sludge formation at exaggerated high Mn content (alloy D). The FIB images (Figure 6) illustrate clearly that huge cavities are formed *via* multiple cracking of the sludge particles, which in turn causes reduced ductility.^[3] Only if both the β -phase and the sludge particles are avoided and the intermetallic phases are kept small through the high cooling rates in HPDC, can crack initiation be transferred to the eutectic silicon particles and high ductility be ensured. Seifeddine *et al.*^[22] showed that the prevention of the β -phase *via* Mn is also possible in permanent die casting. However, they observed a declining elongation to fracture with increasing Mn content because the β -phase is avoided at the expense of the formation of large α -particles which also possess a high cracking susceptibility. Fractographic analyses illustrated that for low Fe and Mn concentrations, eutectic Si particles control the fracture process,^[3,23] but as soon as large intermetallic phases appear they become predominant. Seifeddine *et al.*^[22] concluded that in addition to chemical composition, cooling rate has a substantial influence on phase formation and fracture behavior. Higher cooling rates weaken the negative effect of Mn on the elongation to fracture by reducing the size of the α -phases and transfer the crack initiation from the Fe-containing phases to the Si particles. Assuming a persistent trend, the high cooling rates achieved by HPDC in the present study should definitely favor the Si particles as main crack initiation sites. Wang *et al.*^[24,25] observed simultaneous cracking of Si particles and Fe-containing phases in AlSi7 alloys with low Fe content. They evaluated particle size, particle aspect ratio, and the extent of particle clustering as main factors determining particle cracking. It has also to be considered that the dispersion of the intermetallic phases crucially affects the growth and propagation of microcracks, as it was shown by Cáceres and Taylor.^[26] In Reference 22, it is stated that hardness and elastic moduli of Si particles, β -Al₅FeSi and α -Al₁₅(Fe,Mn)₃Si₂, are comparable. It is therefore supposed that the brittleness of the α - and β -phases is similar to that of silicon particles. Hence, it can be said that for equal size and aspect ratio of eutectic Si and α -phase, as in alloy B, the particle clustering is much more pronounced for Si than for α -Al₁₅(Fe,Mn)₃Si₂, and therefore, cracking should occur in Si particles. Alloy C shows an increased clustering of the α -phase, but this is accompanied by a reduction in their size, which is probably the reason why Si particles are still more critical.

The microstructural observations together with the mechanical tests have shown that if high ductility is required, an increased Fe concentration must be corrected with an accurate balanced amount of Mn to avoid detrimental β -plates on the one hand and large α -particles on the other. Only when the chemical composition of these elements is chosen precisely in a narrow window leading to a full and optimized compensation of Fe, the challenging requirements on the mechanical properties and deformation behavior can be met. The most promising Mn concentration for neutralizing

0.55 wt pct Fe in AlSi10Mg HPDC alloys is in the range of 0.4–0.6 wt pct. Therefore, the requested Mn/Fe ratio should be 0.7 to 1.1. Because it has been shown that high Mn content refines the intermetallic microstructure, we suggest applying a simplified ratio of 1 for optimal iron correction. This suggested ratio differs notably from the values usually discussed in the literature. According to Cao *et al.*,^[10] the Mn content should not be less than half of the Fe content, to assure neutralization. Ji *et al.*^[12] also report that an Mn/Fe ratio of 0.5 is sufficient to avoid the formation of the β -phase in the class of Al-Mg-Si alloys processed in HPDC, and Shabestari^[4] found Fe platelets in alloys with high Fe content only when Mn was <0.2 wt pct. In contrast, Seifeddine *et al.*^[22] recommend a Mn/Fe ratio >2 for total avoidance of Fe-rich platelets. Taylor^[27] indicates that the common Mn/Fe ratio of 0.5 may not always be sufficient to neutralize existing Fe content, and also claims that, if ductility is considered, a critical Fe content in Al-Si alloys is given by $Fe_{crit} = 0.075 Si - 0.05$ [wt pct]. For our alloys with 10.5 wt pct Si, the critical content would be $Fe_{crit} = 0.74$ wt pct. Although Fe concentrations higher than 0.55 wt pct have not been studied in this work, the application of the balanced proportion (Mn/Fe \approx 1) would lead to a Mn content of 0.7 wt pct and result in a segregation factor of 2.1, which is clearly above the postulated limit of 1.8^[9,15] confirmed for HPDC-AlSi10Mg alloys (Figure 3). Consequently, the formation of large particles would have the above-mentioned negative implications for mechanical properties. Lumley *et al.*^[13] claim in their patent application that Mn/Fe = 0.625 to 2.5 provides enhanced fracture resistance in Al-Si-Cu alloys. The lower limit is in good agreement with our proposed ratio for Al-Si-Mg alloys, while the upper limit seems not reasonable for secondary based alloys. Unfortunately, microstructural changes in their suggested wide ratio, especially concerning intermetallic phases, have not been worked out.

The divergence in the assessment of the optimal Mn/Fe ratio is certainly a consequence of processing *via* HPDC at high cooling rates; most other studies have used processing routes more easily available in the laboratory, but which exhibit significantly lower cooling rates.^[4–6,10,11,22,25]

V. CONCLUSIONS

In summary, it has been shown that iron-containing secondary near-eutectic AlSi10Mg cast alloys achieve high ductility through the accurate adjustment of the occurring intermetallic phases and the high cooling rate present in high-pressure die casting.

1. Fracture mechanisms were shown to depend on the chemical composition and fracture initiation to take place at elongated β -phases, eutectic silicon particles, or large α -sludge particles.
2. An Mn/Fe ratio of 1 is recommended to create ‘uncritical’ fine dispersed polygonal α -Al₁₅(Fe,Mn)₃Si₂ particles in HPDC and thereby maintain fracture

- initiation at the eutectic silicon particles (as in primary casting alloys) to produce superior ductility.
- The size of $\alpha\text{-Al}_{15}(\text{Fe},\text{Mn})_3\text{Si}_2$ particles can be decreased by enhanced Mn addition, which increases their liquidus temperatures and generates an increased undercooling and higher nucleation rate for the phase, provided that high cooling rates as in HPDC are applied.
 - The Mn content cannot be extended arbitrarily but is capped by sludge formation at high Mn concentrations; this agrees with the common segregation factor criterion, $SF_{\text{crit}} \approx 1.8$ for typical HPDC processing temperatures.
 - An unexpectedly good combination of yield strength (150 MPa) and ductility (fracture elongation >10 pct) was reached for a class of secondary cast alloys which also exhibit excellent castability and sustainability. These alloys are very promising candidates for complex-shaped, thin-walled castings in the transport industry.

ACKNOWLEDGMENTS

The authors would like to thank AUDI AG and AMAG Austria Metall AG for their financial support of this research project and for permission to publish the results.

REFERENCES

- L.F. Mondolfo: *Aluminium Alloys: Structure and Properties*, 1st ed., Butterworths, London, 1976, pp. 759–805.
- J.G. Kaufman and E.L. Rooy: *Aluminum Alloy Castings: Properties, Processes and Applications*, ASM International, Materials Park, OH, 2004.
- T.O. Mbuya, B.O. Odera, and S.P. Ng'ang'a: *Int. J. Cast Met. Res.*, 2003, vol. 16, pp. 451–64.
- S.G. Shabestari: *Mater. Sci. Eng. A*, 2004, vol. 383, pp. 289–98.
- A. Darvishi, A. Maleki, M. Atabaki, and M. Zargami: *Metall. Mater. Eng.*, 2010, vol. 16, pp. 11–24.
- J.Y. Hwang, H.W. Doty, and M.J. Kaufmann: *Mater. Sci. Eng. A*, 2008, vol. 488, pp. 496–504.
- L.A. Narayanan, F.H. Samuel, and J.E. Gruzleski: *Metall. Mater. Trans. A*, 1994, vol. 25A, pp. 1761–73.
- X. Fang, G. Shao, Y.Q. Liu, and Z. Fan: *Mater. Sci. Eng. A*, 2007, vols. 445–446, pp. 65–72.
- J.L. Jorstad: *Die Cast. Eng.*, 1986, vol. 30, pp. 30–36.
- X. Cao and J. Campbell: *Metall. Mater. Trans. A*, 2004, vol. 35A, pp. 1425–35.
- H.Y. Kim, T.Y. Park, S.W. Han, and H.M. Lee: *J. Crystal Growth*, 2006, vol. 291, pp. 207–11.
- S. Ji, W. Yang, F. Gao, D. Watson, and Z. Fan: *Mater. Sci. Eng. A*, 2013, vol. 564, pp. 130–39.
- R.N. Lumley, D.R. Gunasegaram, M. Gershenzon, and A.C. Yob: Patent Application WO2009/132388A1.
- G. Pucella, A.M. Samuel, F.H. Samuel, H.W. Doty, and S. Valterra: *AFS Trans.*, 1999, vol. 24, pp. 117–25.
- J. Gobrecht: *Fonderie*, 1977, vol. 367, pp. 171–73.
- CompuTherm LLC, Pandat Software Package for Calculating Phase Diagrams and Thermodynamic Properties of Multi-component Alloys, Madison, WI, <http://www.compuTherm.com>.
- W. Kurz and D.J. Fisher: *Fundamentals of Solidification*, CRC Press, Boca Raton, 1998, ISBN 978-0878498048.
- H.I. Laukli: Ph.D. Thesis, NTNU, Trondheim, 2004.
- S. Belmares-Perales, M. Castro-Román, M. Herrera-Trejo, and L.E. Ramirez-Vidaurri: *Met. Mater. Int.*, 2008, vol. 14 (3), pp. 307–14.
- J. Zander, R. Sandström, and L. Vitos: *Comput. Mater. Sci.*, 2007, vol. 41, pp. 86–95.
- O. Vorren, J.E. Evesen, and T.B. Pederson: *AFS Trans.*, 1984, vol. 92, pp. 459–66.
- S. Seifeddine, S. Johansson, and I. Svensson: *Mater. Sci. Eng. A*, 2008, vol. 490, pp. 385–90.
- R. Doglione: *JOM*, 2012, vol. 64, pp. 51–57.
- Q.G. Wang: *Metall. Mater. Trans. A*, 2003, vol. 34A, pp. 2887–99.
- Q.G. Wang, C.H. Cáceres, and J.R. Griffiths: *Metall. Mater. Trans. A*, 2003, vol. 34A, pp. 2901–12.
- C.H. Cáceres and J.A. Taylor: *Metall. Mater. Trans. B*, 2006, vol. 37B, pp. 897–903.
- J.A. Taylor: *Proc. Mater. Sci.*, 2012, vol. 1, pp. 19–33.